14th Australasian Fluid Mechanics Conference
Adelaide University, Adelaide, Australia
10-14 December 2001

Flow Past Elliptical Cylinders at Low Reynolds Numbers

S.A. Johnson, M.C. Thompson and K. Hourigan

Department of Mechanical Engineering
Monash University, Clayton, Victoria, 3800 AUSTRALIA

Abstract

The vortex structures behind 2D elliptical cylinders at low Reynolds numbers were investigated for a Reynolds numbers range of 30 to 200. By varying the aspect ratio of an elliptical cylinder, the geometry varies between the extremes of a circular cylinder and a flat plate normal to the flow. It is ascertained that as the aspect ratio is decreased, the shedding behind the elliptic cylinder changed from steady Karman vortex shedding to a surprising different flow with two distinct regions. The first region situated directly behind the cylinder contained two rows of vortices rolling up from the cylinder with a region of relatively dead flow in between. A convective instability in the flow further downstream causes the two rows of vortices to interact strongly and results in the formation of downstream secondary vortices. It is found that at the transition Reynolds number between the normal Karman vortex wake and the occurrence of secondary vortex shedding, there is a peak in the Strouhal number for a given aspect ratio as well as a local minimum in the drag coefficient. Furthermore, the value of the Reynolds number at the onset of periodic vortex shedding decreased as the aspect ratio decreased.

Introduction

This study of the flow around elliptical bodies examines the nominally two-dimensional wake states generated as the body geometry changes from a flat plate normal to the free stream flow to that of a circular cylinder. In particular, it is concerned with how the vortex structures behind a normal flat plate progress to the Karman vortex structures observed behind a cylinder at low Reynolds numbers. Previous research has examined the flow past cylinders [6] as well as flat plates [2]. The aspect ratio of an elliptical cylinder can be varied to link the flat plate, the circular cylinder and the region between.

The two parameters that were varied in the models were the Aspect Ratio (AR) and Reynolds number (Re). Shown in Figure 1 is the progression of a flat plate to a cylinder where AR=B/A. Therefore, a vertical flat plate has an AR=0 while for a circular cylinder, AR=1. The Reynolds number length scale is A.

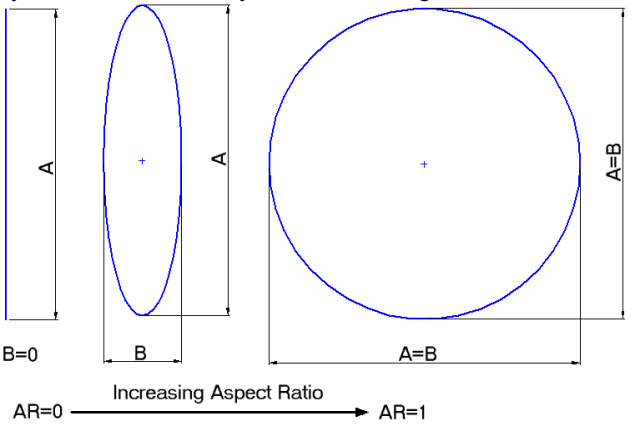

Figure 1: Schematic diagram of changing aspect ratio. Shown is AR=0.0, AR=0.25, and AR=1.0

For this study, a 2D spectral-element method [3] was used to solve the unsteady Navier-Stokes equations governing the fluid flow. Simulations were carried out for aspect ratios ranging from 0.01 to 1.00 and for Reynolds numbers ranging from 30 to 200.

This paper describes the grid set up used for the numerical simulations, accounting for the different aspect ratios, as well as the methodology of data collection to decrease computation time. The vortex structures behind an elliptical cylinder are described for AR=0.5. The effects of Re and AR on the Strouhal number, coefficient of drag and the onset of vortex shedding are also reported here. Finally, validation of results is considered and a conclusion given.

Grid Setup

To capture the vortex structures in the wake of the elliptical cylinder, the grid was required to be fine near and also downstream of the cylinder. Figure 2 depicts the macro-element grid used in the simulations.

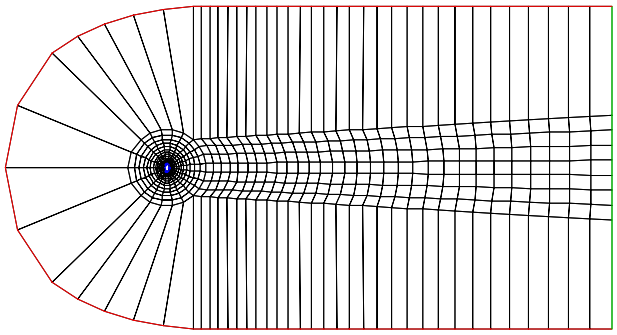

Figure 2: Macro element grid used for AR=0.5. Flow is from left to right.

The discontinuity between the fine and coarse areas in the grid was investigated to ensure it did not induce errors into the solution. If the discontinuity remained in the free stream flow where the velocity gradients were small, the results remained unaffected. To accommodate different aspect ratio elliptical bodies, the grid was stretched in the circular grid region as shown in Figure 3. The same numbers of macro-elements were used near the surface of the ellipse to capture the boundary layer.

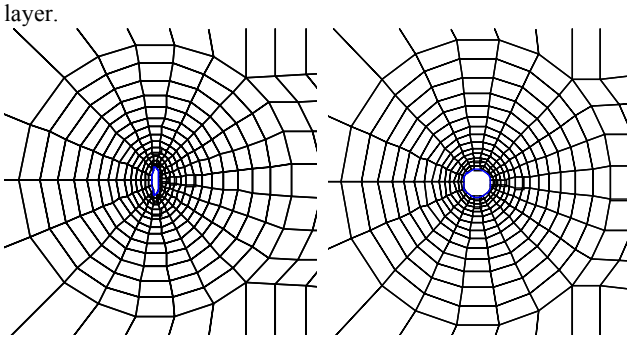

Figure 3: Grid stretching near the object to account for the different AR used. The grid is for AR=0.125 (left) and for AR=1.00 (right).

The inlet boundary condition of uniform velocity was assigned to the top and bottom edges and on the circular left boundary. The side boundaries were positioned 20A away from the cylinder. The right-hand boundary was specified as an outlet and placed 55A downstream. The ellipse was specified as a no-slip wall, with the curvature of the walls calculated to produce a smooth surface for the elements used in the spectral-element numerical code.

Data collection

Simulations were run in three steps. The models were first run using 4x4 nodes per element (NPE). (Each macro-element shown in Figure 3 is subdivided internally into nx x ny nodes. In this case, nx=ny=4.) This resolution is kept for 300 non-dimensional time units to allow sufficient time to evolve the flow and for the onset of vortex shedding. (Time is non-dimensionalised by the upstream velocity and ellipse diameter A). After this time, the results were mapped onto a grid with 49 NPE to increase the accuracy. However, due to the change in resolution, the models needed to be run a further 50 units to remove transient effects. Finally each simulation was run for a further 200 time units to collect data for analysis; with data for flow visualisation being collected every 0.25 units, and data recording the forces on the elliptical cylinder every 0.1 units. Note that the shedding period is typically between 5 and 10 dimensionless time units.

Results

Types of shedding

Six different types of flow patterns were categorised in the simulations. These were; steady flow, Karman-type vortex shedding, symmetric wake, transitional vortex shedding, steady secondary shedding and unsteady secondary shedding. To explain the shedding types that occur, vorticity plots were utilised to visualise the different forms of shedding on an elliptical cylinder with AR=0.5 as the Reynolds number is increased from 40 up to 250. Even though Re=250 is above the range this paper examines, the shedding patterns are the same at lower Re and higher AR. Vorticity is shown in the range of –1 to 1 with positive vorticity indicated with solid lines and negative vorticity as dashed lines.

Figure 4: Steady flow occurring at Re=40 for AR=0.5.

At Re=40 and Re=42.5, steady flow occurred around the body with no shedding as shown in Figure 4. In this Re regime, flow was below the critical Reynolds number where the flow becomes unsteady.

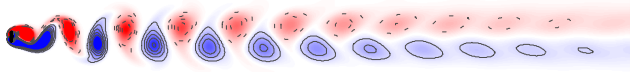

Figure 5: Vortex shedding occurring at Re=75 for AR=0.5.

Between Re=45 and Re=75 shedding occurs as seen in Figure 5. The vortex shedding forms a von Karman vortex street. As can be seen in Figure 5, the vortices further downstream start to diffuse and skew. Tests were conducted to check if the skew was induced by effects from the outlet boundary condition, but moving the outlet position did not affect the results. Instead, the skewing of the vortices is due to reduced x-velocity in the region behind the cylinder, which is lower than the free stream velocity. This causes the vortices to skew due to the relative velocity difference between their top and bottom. This feature is also observed in the experimental flow visualisations [4] which show the similar skew of the vortex cores occurring behind a cylinder far downstream at Re=100.

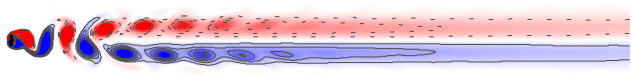

Figure 6: Symmetric wake occurring at Re=125 for AR=0.5.

As the Reynolds number was increased, the region of skewed flow became stronger. As a result, the flow develops into a region where the positive and negative vortex cores diffused together into two rows extending downstream to the outlet. These rows formed two shear layers between the region of slower flow behind the cylinder and the free stream velocity. As the Reynolds number is increased the symmetric wake region occurs closer to the cylinder. This is highlighted in the differences between Figure 6 and Figure 7.

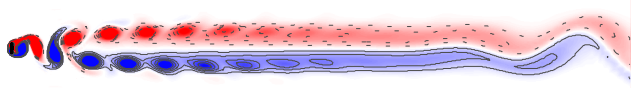

Figure 7: Transitional shedding occurring at Re=150 for AR=0.5.

At Re=150, a convective instability forms in the symmetric wake shear layers near the outlet of the simulation. In this case the two shear layers do not interact with each other and there is still a region where the vorticity is zero. This secondary shedding remained periodic with a frequency less than shedding frequency of the cylinder. Increasing the Re further caused the amplitude of the secondary oscillations to increase. The onset of the convective instability began closer to the elliptical cylinder since the shear layer was stronger. It is expected that the symmetric shear layers will become unstable for all cases beyond a critical wavelength. However for lower Re, this evidently would occur more than 55A away from the cylinder and was not observed since it was outside the simulation.

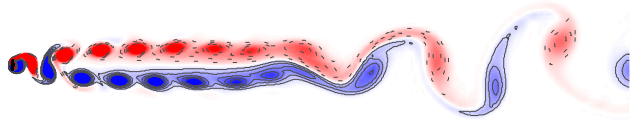

Figure 8: Steady secondary shedding occurring at Re=175 for AR=0.5.

For Re=175 and Re=200, the vortex shedding patterns have changed considerably as shown in Figure 8. The symmetric wake regime decreases considerably with a secondary vortex pattern occurring downstream. This may be due to the convective instability occurring closer to the elliptical cylinder. At this position, the vortices shed from the cylinder have not completely diffused and start to interact. This interaction, caused by the convective instability, forces two of the vortices from one of the rows to roll up into one vortex and move downstream. This action then alternates between the two rows as the secondary vortices are shed. The average x-velocity along the centre line is now negative in some regions inside the parallel rows of vortices. This recirculation inside the parallel rows leads to a secondary shedding. This can be seen later in Figure 15, which shows mean x-velocity profiles on the centre line.

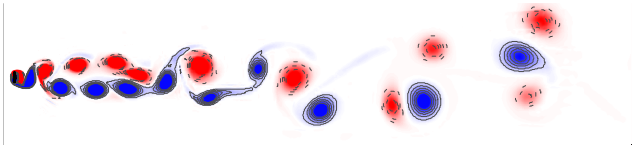

Figure 9 Unsteady secondary shedding occurring at Re=250 for AR=0.5.

At Re=250, the secondary shedding is no longer occurring in pairs. As shown in Figure 9, the secondary shedding is occurring with no distinct pattern. The frequency due to the convective instability does not appear to be related to the primary shedding frequency. As a result, the secondary shedding does not display a continuous pattern over time. The instantaneous time shot in Figure 9 shows two triple groups consisting of two negative vortices and one larger positive vortex. However, the next triple grouping has the opposite vortex sign, displaying an inconsistency in the pattern. Vortex pairs were also observed to shed intermittently.

Shedding patterns at different Re and AR

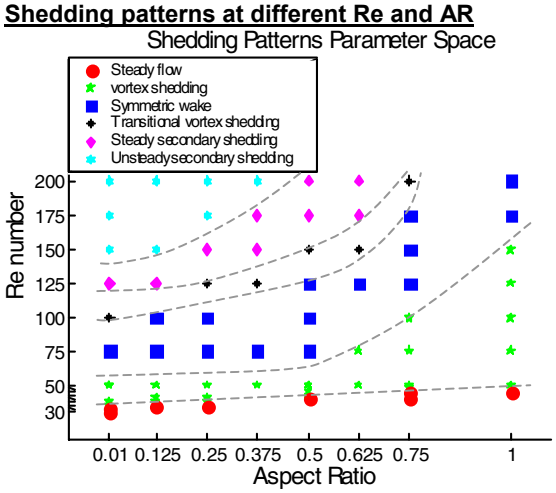

Figure 10. Parameter space graph showing shedding types for a given Re and AR. Dashed lines are included as an aid for visualising boundaries.

Shown in Figure 10, is the parameter space graph indicating the types of shedding that occur at different Re and AR. As the AR decreased and the Re increased, the shedding pattern changed from a Karman vortex street to unsteady secondary shedding. For increasing AR, the onset of secondary vortices occurs at higher Re. However, secondary vortices were not observed for AR=1 which was tested up to Re=300. It must be recognised, that above Re≈180 for a circular cylinder, 3D effects occur in the flow behind the cylinder [7]. Decreasing the aspect ratio will decrease the Re at which the 3D effects occur, causing these results only to be visualised using purely 2D experiments such as a soap film bubble visualisation [5]. A Karman Vortex Street was observed for low AR, however, only at Re<75. Linear floquet stability analysis [1] to determine if the flow is 3D is yet to be conducted. However it is expected that in symmetric wake regime, this feature is would not be present since there would be greater diffusion in a 3D model.

Strouhal Profiles

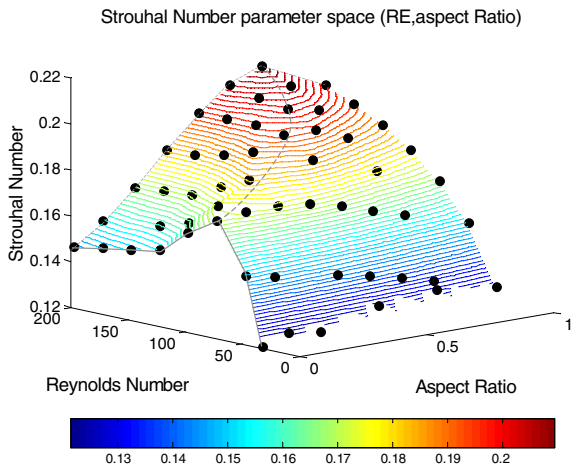

Figure 11 Parameter space model of the Strouhal number with respect to the AR and Re. The dashed line indicates in the ridge that occurs for the Strouhal number as Re is decreased Black dots indicate calculated data points.

Once steady periodic shedding was achieved on all models, the Strouhal number was calculated for the primary shedding occurring around the cylinder using the cyclic lift force. Shown in Figure 11, is the Strouhal number parameter space graph. For Re>100, there was a peak in the shedding frequency as the AR decreased. This peak corresponded with the onset of transitional shedding. At Re<100, there was no steady secondary shedding, so the Strouhal number was highest for the low AR elliptical cylinders as shown in Figure 12. For AR=1.00 the Strouhal number closely follows other results below Re≈180.

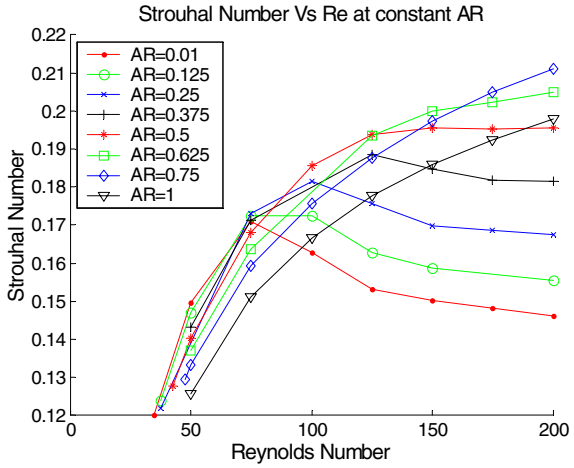

Figure 12 Variation in Strouhal number for different aspect Ratios.

Drag

Shown in Figure 13, is the drag from the elliptical cylinders as a function of Re.

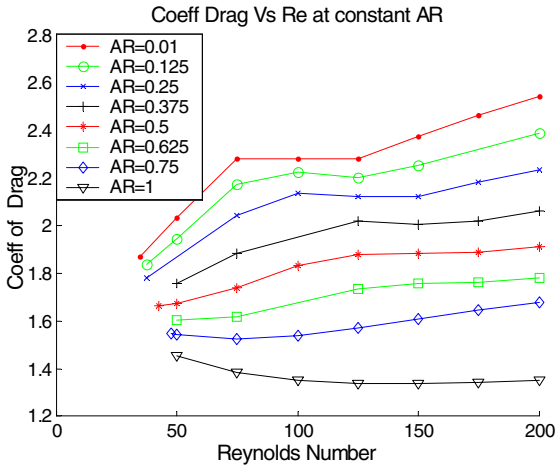

Figure 13 Variation in the drag coefficient for different aspect ratios.

The general trend for a given AR is an increase in drag as the Re increases. This is true for all cases except the circular cylinder where the drag decreases. By increasing the Re, the pressure drag increases and the viscous drag decreases. For elliptical cylinders, the viscous drag is smaller than a circular cylinder since the viscous drag acts parallel to the surface of the elliptical cylinder while the pressure drag is greater since it acts normal to the surface. AR=0.001 always has greater drag than AR=1.00 for a given Re since the pressure drag is more dominant. For AR=1.00, by increasing the Re, the drag decreases since the viscous drag component which is significant at low Re, decreases at higher Re. At Re>175, the drag increases slightly which was not observed in experimental results. This could be due to the fact the 3D effects are not considered in the 2D model or there could be round off error in the calculation of the drag since it only increases by 0.0132.

For AR=0.125 and AR=0.25, there is a local minima at Re=125 and Re=150 respectively. This point coincides with the transition from symmetric wake to secondary shedding. This trend continues with AR=0.01, 0.25, 0.5 and AR=0.625. This local minimum is due to a change in the pressure drag and not the viscous drag.

Onset of Vortex Shedding

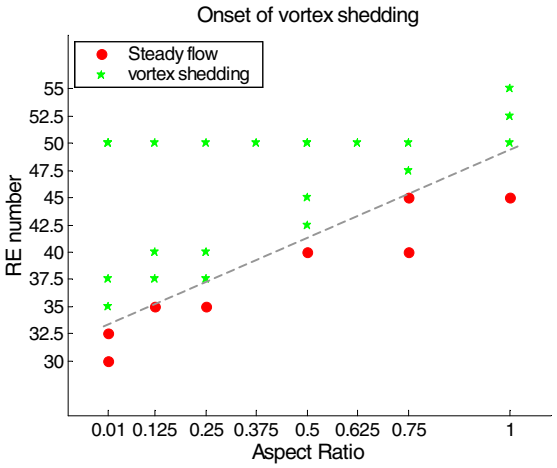

Figure 14 Onset of vortex shedding for different AR elliptical bodies. Dashed lines are included as an aid for visualising boundaries.

For low Re, the flow changes from steady to periodic vortex shedding. Figure 14 is the lower regime of Figure 10, showing clearly the onset of shedding. To determine the Re at which the vortex shedding first occurred, the Re was increased until vortex shedding occurred. The Re was then decreased to the previous Re to check if the vortex shedding decayed. As shown in Figure 14, as the AR, decreased, the Re at which the vortex shedding occurred decreased. For AR=0.01, the critical Re is between 32.5-35 whereas for AR=1.00, the critical Re is between 45 and 50. A straight line was fitted to results indicating a linear decrease in the critical Re with AR. However, this needs to be investigated further to confirm this observation.

Validation

Grid Resolution Study

A grid resolution study was conducted on AR=0.25 at Re=250 to check the number of NPE. This model was used since velocity gradients would greater at high Re and low AR. The NPE was increased from 49 to 64 and then to 81 with the average velocity field being compared. The average x-velocity plotted in Figure 15 shows very little change. The small change in results was not sufficient to warrant an increase as it would result in a prohibitive increase in computation time.

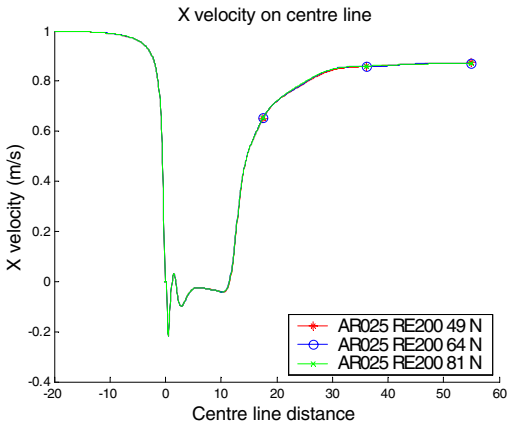

Figure 15 Time-averaged x-velocity on the y=0 centreline for NPE=49, 64 and 81. Note that the time-averaged velocity is negative, indicating recirculation.

Fluent comparison

Concern was raised that this flow could be a numerical error due to the spectral-element numerical code. Modelling was carried out using Fluent 5 to confirm the results. Figure 16 shows vorticity contours flow field for AR=0.25 at Re=250 which is similar to the spectral-element model shown in Figure 8.

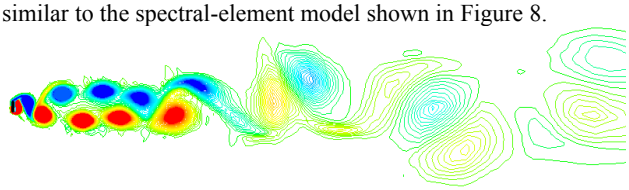

Figure 16 Vorticity contours for AR=0.25 at Re=250 using Fluent 5.

3D Effects

For a circular cylinder, the flow field becomes 3D above Re≈180. Since the onset of vortex shedding occurs at lower Re as the AR decreases, it is assumed that the Re at which flow becomes 3D also decreases. Studies done on a normal flat plate at Re=250 showed a substantially different flow field when a 3D flow field is modelled [2]. It is expected that the shedding pattern at lower Re, would also be different. However this needs to be confirmed using 3D modelling.

Conclusion

This paper has presented results for flow around an elliptical cylinder with varying aspect ratios and Reynolds numbers. The flow structures have been discussed as well as a parameter space model indicating the shedding types for given Re and AR. They have shown substantial change in the shedding types caused by the convective instability interacting with the vortex shedding occurring behind the cylinder. As seen in Figure 11 and Figure 13, there is a change in the drag and Strouhal number when steady secondary shedding occurs. Further research is still needed to study 3D effects.

Acknowledgements

Shaun Johnson gratefully acknowledges the financial support of the Monash departmental scholarship.

References

[1] Barkley, D & Henderson, R.D. Three-dimensional Floquet stability analysis of the wake of a circular cylinder, Journal of Fluid Mechanics, 322, 1996, 215-241.

[2] Najjar F.M. & Balachander, S., Low-frequency unsteadiness in the wake of a normal flat plate. Journal of Fluid Mechanics, 370, 1998, 101-147.

[3] Thompson, M.C., Hourigan, K., Sheridan, J., Three-dimensional instabilities in the wake of a circular cylinder, Experimental and Thermal Fluid Science,12, 1996, 190-196.

[4] Van Dyke, M. (editor), An Album of Fluid Motion, The Parabolic Press, 1982.

[5] Wen, C.Y. & Lin, C.Y., Tow-dimensional vortex shedding of a circular cylinder, Physics of Fluids, 13(3), 2001, 557-560

[6] Williamson, C.H.K., Advances in our understanding of vortex dynamics in bluff bodies, Journal of Wind Engineering, 69-71 1997, 3-32.

[7] Williamson, C.H.K., Three-dimensional wake transition, 1996, Journal of Fluid Mechanics, 328, 1996, 345-407.